

Safe Multitask Molecular Graph Networks for Vapor Pressure and Odor Threshold Prediction

Shuang Wu^{*1}, Meijie Wang², and Lun Yu^{†2}

¹Department of Civil, Environmental and Geomatic Engineering, University College London, London WC1E 6AP, United Kingdom

²Metanovas Biotech, Inc., San Francisco, CA 94108, USA

January 26, 2026

Abstract

1 Introduction

Vapor pressure (VP) and odor threshold (OP) are two complementary molecular properties that critically link chemical structure to human exposure and environmental impact. *Vapor pressure* governs a compound’s propensity to partition into the gas phase, underpinning process safety, formulation design, and environmental transport. Conversely, *odor threshold* quantifies the minimum airborne concentration at which humans perceive an odor, making it central to nuisance control and risk assessment. Jointly modeling VP and OP is therefore highly attractive: VP determines *whether* a molecule is likely to reach the nose, whereas OP modulates *how easily* it will be perceived once airborne. However, unlike the relatively stable thermophysical measurements of VP, OP labels are notoriously heterogeneous across media and protocols, often rendering them noisy and posing unique challenges for machine learning [1, 2, 3].

In molecular property prediction, early pipelines relied on fixed fingerprints and hand-crafted descriptors (e.g., ECFP/Morgan, TPSA, logP) coupled with linear models or tree ensembles [4]. Graph neural networks (GNNs) now dominate due to their ability to operate directly on molecular graphs and learn task-relevant representations via message passing [5]. Graph Isomorphism Networks (GIN) improved expressivity by aligning with the Weisfeiler–Lehman test [6], GINE incorporated edge features explicitly to better encode chemistry [7], and Principal Neighbourhood Aggregation (PNA) combined multiple aggregators and

^{*}ucesswu@ucl.ac.uk

[†]Corresponding author: lunyu@metanovas.com

degree-aware scalers to improve robustness across degree distributions and local topology shifts [8].

Crucially, evaluation protocol strongly influences conclusions. Random splits inflate apparent generalization by allowing substantial scaffold overlap between train and test. Community best practice increasingly favors *Bemis–Murcko scaffold* splits and, where applicable, time splits to better approximate prospective performance and out-of-distribution (OOD) behavior [9, 10, 11, 12]. Under scaffold-split OOD evaluation, we observe that concatenating strong fingerprints with graph features can “overshadow” graph encoders and hurt OOD robustness, whereas graph-dominant representations with chemistry-aware edge features are more stable.

Multitask learning (MTL) promises data efficiency by sharing a backbone across related endpoints [13, 14]. In cheminformatics, MTL has helped when tasks are correlated and labels are scarce [15]. However, *negative transfer* arises when gradients from one task impede another, especially under task imbalance (unequal label counts) and label-noise asymmetry, both common for VP (cleaner) and OP (noisier, sparser) [16]. To mitigate conflict, optimization-based strategies project or reweight task gradients (e.g., MGDA, PCGrad) [17, 18], uncertainty-based weighting adapts task losses on-the-fly [19], and training schedules stagger task activation or apply asymmetric updates. A practical and robust paradigm for safety-critical primary tasks is what we term *safe multitask*: delay the auxiliary task, warm up its loss weight at a small target λ , optionally prevent its gradients from modifying the backbone (detach/gradient isolation), and—importantly—maintain *per-task early stopping and checkpoints* so each endpoint can “keep” its own best model even if later updates are harmful.

In this work we study joint VP–OP modeling under strict scaffold-split OOD. We compare GINE and PNA backbones with chemistry-aware edge features and temperature conditioning, and we formalize a simple, reproducible *safe multitask* training regimen: (i) phase 1 trains VP only; (ii) phase 2 activates OP with linear λ -warmup at a small final weight; (iii) optional gradient isolation for OP to protect the shared backbone; and (iv) *per-task* validation and checkpoints (ACS-style) so each task preserves its own optimum. We report multi-seed means and standard deviations, ablations over λ , warmup length, detach, and checkpoints, and residuals versus similarity to diagnose OOD behavior. Empirically, PNA with safe multitask achieves competitive VP accuracy without sacrificing the primary task, while OP serves as a lightweight regularizer rather than a co-driver of the backbone. Our contributions are:

1. A reproducible, graph-dominant baseline for VP/OP under scaffold-split OOD with chemistry-aware edge features and temperature input;
2. A practical *safe multitask* regimen (delayed activation, small- λ warmup, optional gradient isolation, per-task checkpoints) that reduces negative transfer in imbalanced, noisy multitask settings;
3. A systematic comparison of GINE vs. PNA and light vs. rich molecular features, with ablations and diagnostics that clarify when auxiliary OP helps—and how to ensure it does not hurt—the primary VP task.

Notation. Throughout, we report normalized-space metrics (MSE/MAE/ R^2) under Be-

mis–Murcko scaffold splits and provide de-normalized errors where relevant.

2 Related Work

2.1 Molecular Property Prediction on Graphs

Classical cheminformatics relied on fixed fingerprints (e.g., ECFP/Morgan) and physico-chemical descriptors paired with linear models or tree ensembles [4, 20]. End-to-end graph neural networks (GNNs) supplanted these pipelines by learning representations directly from molecular graphs via message passing [5]. Among expressive architectures, GIN aligns with the Weisfeiler–Lehman hierarchy [6], GINE injects bond features into the message function to encode chemistry [7], GAT introduces attention over neighbors [21], and SchNet uses continuous-filter convolutions tailored to atomistic interactions [22]. PNA aggregates with multiple statistics and degree-aware scalers for robustness under heterogeneous local topology [8], while transformer-style graph models (e.g., Graphomer) have further pushed the frontier on diverse graph benchmarks [23].

Pretraining and self-supervision have improved data efficiency: contrastive and mutual-information objectives (e.g., InfoGraph) [24], large-scale self-supervised graph transformers (GROVER) [25], and strong supervised baselines such as Chemprop (message passing with RDKit features) [26]. Practical regularization for deep GNNs includes stochastic edge dropping (DropEdge) [27] and weight averaging (SWA/Polyak averaging) to find wider optima [28, 29]. The community has converged on standardized graph benchmarks and protocols (OGB, MoleculeNet) to compare models fairly [30, 11].

2.2 Evaluation Protocols and OOD Generalization

Evaluation strongly shapes perceived progress in molecular ML. Random splits often leak Bemis–Murcko scaffolds across train/test, inflating apparent accuracy [9, 11]. Time splits probe prospective performance by respecting chronology [10, 31]. Recent analyses detail pitfalls such as data leakage, insufficiently strict splits, and descriptor-induced shortcuts, advocating realistic OOD protocols and careful reporting [32, 12]. Our study follows these recommendations by using scaffold splits and by reporting residuals versus similarity to diagnose shortcircuiting.

2.3 Odor Threshold Modeling

Odor threshold (OP) prediction is difficult due to heterogeneity across media (air/water), protocols, and sensory panels; reported thresholds for a single analyte can span orders of magnitude [3, 2, 33]. Large-scale studies have shown that chemical features can predict aspects of human olfaction, albeit with ceilings imposed by label noise and perceptual variability [1]. In practice, robust targets (e.g., log-scaled thresholds), medium-specific standardization, and noise-tolerant losses (e.g., Huber) are advisable [34, 35, 36]. Compared with thermophysical endpoints like vapor pressure (VP), OP data are typically smaller and noisier, making them a natural auxiliary rather than a primary training signal.

2.4 Multitask Learning and Negative Transfer

Multitask learning (MTL) seeks inductive transfer by sharing representations across related endpoints [13, 14]. In cheminformatics, MTL can help when tasks share mechanisms or chemical substructures, but gains are uneven and sensitive to relatedness, balance, and noise [15]. A central failure mode is *negative transfer*: gradients from one task hinder another, especially under task imbalance or asymmetric label noise [16, 37].

Three families of remedies recur. (i) **Gradient-level conflict mitigation** projects or reweights task gradients, as in multi-objective optimization (MGDA) [17] and gradient surgery (PCGrad) [18]. (ii) **Adaptive loss balancing** scales task losses by uncertainty or learning dynamics, e.g., Kendall et al.’s homoscedastic uncertainty weighting [19] and GradNorm [38], or dynamic weight averaging [39]. (iii) **Curriculum/scheduling and asymmetry** delays auxiliary activation, warms up its weight λ , and optionally isolates its gradients from the backbone (detach/clip), keeping the auxiliary as a lightweight regularizer instead of a co-driver. Our *safe multitask* recipe follows this third line while combining it with per-task validation and checkpoints (ACS-style safeguarding): the primary (VP) first establishes a stable backbone; the auxiliary (OP) is then introduced with a small, linearly warmed λ , and its gradients are constrained; finally, each task preserves its own best checkpoint to avoid late-stage interference. Robust regression (Huber/winsorization) [34, 36] and, when appropriate, heteroscedastic heads [40] complement these strategies under noisy labels.

2.5 Physical and Perceptual Coupling between Vapor Pressure (VP) and Odor Threshold (OP)

Volatility and odor perception form a causal chain from *generation of vapor* to *human detection*. The **vapor pressure** (VP) of a compound governs its propensity to partition into the gas phase, thereby setting the upper bound of airborne concentration near sources; the **odor threshold** (OP) quantifies the minimum concentration at which a typical human panel detects the odor with a given probability. In other words, VP answers *can the molecule reach the nose?*, whereas OP answers *once present, how easily is it perceived?*

For a dilute solution or neat phase at temperature T , the near-source gas-phase concentration C_{air} scales with VP via Raoult’s/Henry’s law approximations:

$$C_{\text{air}} \approx \frac{y P_{\text{tot}}}{RT} \quad \text{with} \quad y \approx \begin{cases} x \frac{P^*(T)}{P_{\text{tot}}}, & (\text{Raoult, ideal solution}) \\ H^{-1}(T) a, & (\text{Henry, dilute/aqueous}), \end{cases} \quad (1)$$

where $P^*(T)$ is the pure-component vapor pressure (or activity-modified VP), x the liquid-phase mole fraction, a the activity, $H(T)$ Henry’s constant, P_{tot} ambient pressure, and R the gas constant. Thus, higher VP (or lower H) generally increases attainable C_{air} for a given matrix and source loading. Temperature modulates P^* exponentially (e.g., Antoine or Clausius–Clapeyron), motivating our temperature channel.

Psychophysically, detection probability follows a sigmoidal (psychometric) function of

concentration, with a 50% point near the *odor threshold* OT:

$$\Pr(\text{detect} \mid C) = \frac{1}{(1 + (C_{50}/C)^\gamma)}, \quad \text{OP} \approx \log_{10} C_{50}, \quad (2)$$

where γ is the slope parameter capturing panel sensitivity dispersion. Reported thresholds vary by *medium* (air/water), protocol, and panel composition, inducing heteroscedastic label noise. We therefore standardize OP by medium (OA/OW) and apply robust training (§3.4).

Despite different endpoints, VP and OP share chemical determinants (functional groups affecting volatility, polarity, hydrogen bonding, and receptor interaction motifs). A shared graph backbone can encode structure–property regularities useful to both tasks, while the OP head learns perceptual calibration on top of volatility–driven exposure. However, OP labels are *noisier and sparser* than VP, so naive joint training risks *negative transfer*. This motivates our *safe multitask* design: (i) VP-first training to establish a robust backbone; (ii) delayed, small- λ OP activation; (iii) optional gradient isolation from OP to the backbone; and (iv) per-task validation/checkpoints to preserve each task’s optimum.

In practical applications (e.g., emission abatement, formulation screening), a compound with high VP but very high OP may be *less noticeable* than a compound with moderate VP and very low OP. Joint modeling allows ranking by composite criteria such as C_{air}/C_{50} or predicted detection probability (2), once C_{air} is estimated from VP (1) for a given scenario.

We recommend a schematic showing: (1) liquid/solid source \rightarrow gas phase (arrow labeled “VP, $P^*(T)$ ”); (2) transport box (dilution/ventilation); (3) nose/sensory panel (sigmoid curve with OP). An inset can illustrate how temperature shifts VP curves and detection probability.

2.6 Positioning of This Work

We position our contribution at the intersection of chemistry-aware graph modeling and pragmatic MTL. Concretely, we (i) adopt scaffold-split OOD evaluation [9, 32, 11], (ii) use modern GNNs with edge-aware message passing and degree-robust aggregation (GINE/PNA) [7, 8], (iii) treat OP as an auxiliary, noisy signal regularizing a VP-centric backbone, employing robust losses and a *safe multitask* schedule [19, 38, 39], and (iv) apply simple yet effective training stabilizers (DropEdge, weight averaging) where beneficial [27, 28]. This design aims to retain the upside of inductive sharing while minimizing negative transfer in realistic, imbalanced, and noisy molecular property settings.

3 Data and Splitting

3.1 Data Sources and Processing

We consider two complementary endpoints: (i) **vapor pressure (VP)** from curated physico-chemical tables and internal measurement sheets, containing SMILES, measurement `temperature` (in K), and `log_vp` (typically $\log_{10} P$ in Pa or mmHg); and (ii) **odor threshold (OP)** from a consolidated table of literature records, harmonized to molecule-level entries via a mapping from Chemical Abstracts Service (CAS) registry numbers to canonical SMILES

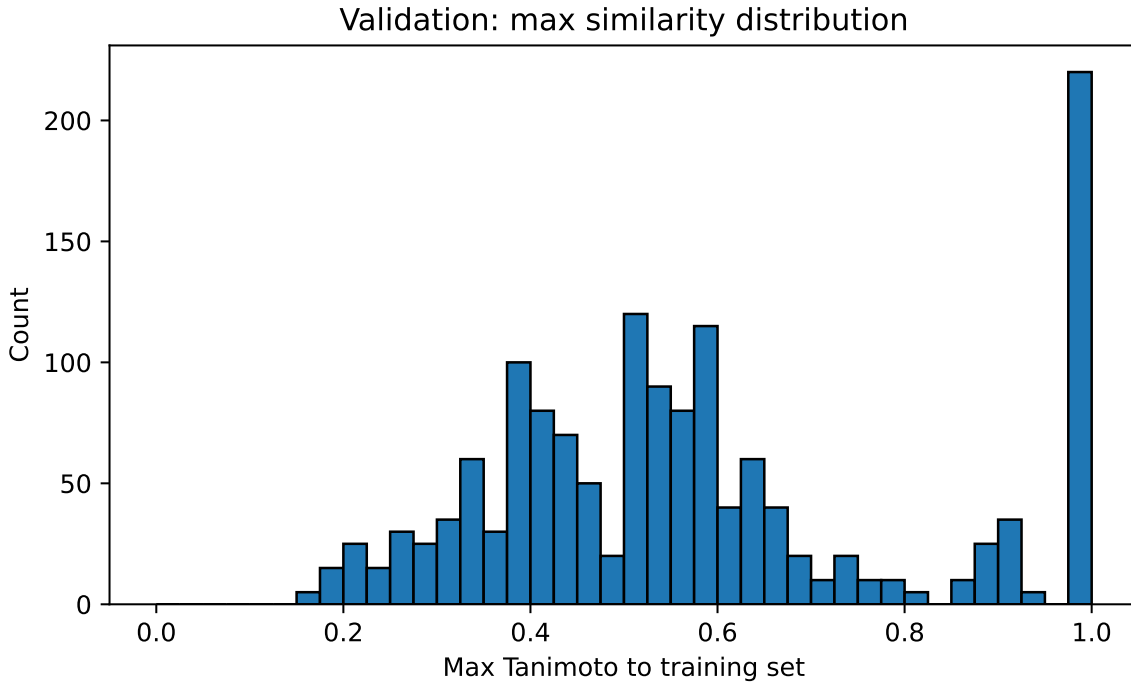


Figure 1: Validation molecules’ maximum Tanimoto similarity to the training set (ECFP4). The mass is centered around 0.35–0.65 and a visible low-similarity tail confirms the out-of-scaffold setting. This motivates reporting OOD robustness rather than random-split performance.

(RDKit). Each OP record is annotated by `medium` $\in \{\text{air, water}\}$ and bibliographic provenance [3, 2, 1, 33]. We denote the two OP targets as `OA` (air) and `OW` (water), expressed as $\log_{10}(\text{threshold})$.

All structures are sanitized and canonicalized (RDKit), salts/solvents are stripped when unambiguous, and explicit hydrogens are removed for graph construction. Duplicate entries arising from synonyms/CAS aliasing are resolved by canonical SMILES; for OP, when multiple thresholds exist for the same (molecule, medium), we adopt a robust *median* aggregator in log space after unit harmonization.

VP values are converted to a single pressure unit (Pa) before \log_{10} transform; temperature is converted to Kelvin. OP thresholds reported in diverse units (e.g., ppb, mg/m³, $\mu\text{g/L}$) are converted to molar or mass concentration and then mapped to \log_{10} -space. We retain the original raw fields to allow back-transformation for reporting in native units.

3.2 Molecular Graph Representation and Target Normalization

For all models we use a graph-dominant representation with chemistry-aware edges. Each molecule is encoded as an attributed graph with the following feature sets:

- **Atoms (A20).** A 20-dimensional vector per node including element type (C, N, O, F, Cl, Br, I, S, P, other), degree, formal charge, hybridization ($\text{sp}/\text{sp}^2/\text{sp}^3/\text{other}$), aromaticity, ring membership, total hydrogen count, and a chirality-center flag.

- **Bonds (E17).** A 17-dimensional vector per edge including bond order (single/double/triple/aromatic), conjugation, ring membership, stereochemistry (NONE/ANY/Z/E/CIS/TRANS), and ring-size indicators (3/4/5/6/ ≥ 7).

Compared with the minimal 4-dimensional node and 6-dimensional edge encodings used in earlier baselines, A20/E17 inject richer local chemistry into message passing and improve robustness under scaffold-split evaluation [7, 8]. For VP we additionally provide a scalar **temperature channel** t at the graph level (standardized on the training set) that is concatenated after graph readout.

Targets are normalized using *training-fold* statistics to avoid leakage [32]. Let $\tilde{y} = (y - \mu)/\sigma$ with (μ, σ) computed on the training fold; then

$$\tilde{y}^{\text{VP}} = \frac{\log_{10} P - \mu_{\text{VP}}}{\sigma_{\text{VP}}}, \quad (3)$$

$$\tilde{y}^{\text{OA}} = \frac{\log_{10} \text{OT}_{\text{air}} - \mu_{\text{OA}}}{\sigma_{\text{OA}}}, \quad \tilde{y}^{\text{OW}} = \frac{\log_{10} \text{OT}_{\text{water}} - \mu_{\text{OW}}}{\sigma_{\text{OW}}}. \quad (4)$$

In the multitask dataset, each graph carries a dense \tilde{y}^{VP} and an OP target together with a binary mask $m \in \{0, 1\}$; samples with $m=0$ do not contribute to the OP loss. When OA/OW are pooled into a single OP target, we use the per-molecule *median* in log space; when they are modeled jointly, two heads and two masks are stored.

Given the heavy-tailed and heterogeneous OP labels, we apply mild **winsorization** in log space (e.g., clipping the bottom/top 2–2.5% quantiles per medium) and use a robust loss (Huber) in OP single-task ablations. For the joint VP+OP setting reported in the main experiments, we primarily use MSE on standardized targets and cross-check with Huber in sensitivity analysis [34, 35, 36].

When measurement uncertainties or panel variances are reported, they are stored as an optional σ channel per OP record and can be used for uncertainty-aware weighting in auxiliary losses [19].

We first construct molecule-level records (unique canonical SMILES) with all available endpoints, then apply the scaffold split (Section 3.3), and finally materialize per-endpoint examples with masks. This ensures that VP and OP instances of the same molecule are always assigned to the *same* fold.

3.3 Scaffold Split and Time-Aware Evaluation

Random splits allow substantial Bemis–Murcko scaffold overlap between train and test, inflating apparent performance. To emulate out-of-distribution (OOD) generalization, we therefore enforce scaffold disjointness between train/validation/test [9, 11, 32] and, where timestamps exist, add light chronology checks to rule out unrealistic “future-to-past” leakage [10, 31].

Given canonical SMILES for all molecules, the scaffold split is constructed as follows:

1. **Scaffold extraction.** We compute Bemis–Murcko frameworks (RDKit) and group molecules by identical scaffold.
2. **Capacity-aware bin packing.** Scaffold groups are sorted by size (descending) and greedily assigned to *train*, *val*, or *test* to approach an 80/10/10 ratio. This “capacity–

“first” heuristic keeps fold sizes balanced and avoids degenerate tiny folds. All endpoints (VP, OA/OW) for the same molecule are forced into the *same* fold.

3. **Freeze splits.** The resulting fold assignment is persisted, keyed by canonical SMILES, so that all experiments and future work reuse identical splits.

For each split we publish the following leakage and OOD diagnostics:

- **Identity overlap:** exact SMILES intersection between train and val/test (expected 0).
- **Scaffold overlap:** fraction of test scaffolds seen in train (expected 0 by construction).
- **Similarity hardness:** for each val/test molecule, the *maximum* ECFP4 (radius 2) Tanimoto similarity to any training molecule [4]. We report summary statistics (median, IQR, 95th percentile) and include a histogram/density plot to visualize the OOD regime.
- **Residuals vs. similarity:** scatter of absolute residuals against max-similarity to detect shortcircuiting; flat or weakly sloped trends are desirable.

Where record dates were available (e.g., measurement years for VP tables or publication years for OP sources), we performed a simple sanity check to confirm that validation/test molecules do not systematically precede the training molecules in time, but we did not otherwise use these dates as model inputs or for a dedicated time-based split.

For reproducibility, our code release includes the processed scaffold splits as ready-to-use PyTorch Geometric datasets together with scripts for rebuilding them from the raw sources.

3.4 Outlier Detection and Robustness

Odor-threshold (OP) labels are heterogeneous across media and protocols; even after unit harmonization, the empirical distribution of $\log_{10}(\text{OT})$ is heavy-tailed with occasional conflicts across sources. Naively training with ℓ_2 amplifies the influence of these extremes and degrades generalization. We therefore combine *distribution shaping* (winsorization) with *robust estimation* (Huber loss), following classical robust statistics [34, 35, 36].

Let z denote $\log_{10}(\text{OT})$ within a medium (OA/OW). For each medium we compute empirical quantiles q_α and $q_{1-\alpha}$ with $\alpha \in [0.02, 0.025]$ (selected on a held-out fold), and define the winsorized target

$$z^{\text{win}} = \begin{cases} q_\alpha, & z < q_\alpha, \\ z, & q_\alpha \leq z \leq q_{1-\alpha}, \\ q_{1-\alpha}, & z > q_{1-\alpha}. \end{cases}$$

Winsorization is applied *only* on the training fold to prevent leakage. For VP we did not observe comparable heavy tails and thus do not winsorize by default.

Within each training fold and per endpoint, we standardize by robust statistics:

$$\tilde{y} = \frac{y - \text{median}(y)}{\max(\text{MAD}(y), \varepsilon)}, \quad \text{MAD}(y) = \text{median}(|y - \text{median}(y)|),$$

with $\varepsilon = 10^{-8}$ for numerical stability. We report both robust-scaled metrics and (when needed) metrics re-mapped to the original unit space.

During training we optionally replace MSE with the Huber loss for OP:

$$\mathcal{L}_\delta(r) = \begin{cases} \frac{1}{2}r^2, & |r| \leq \delta, \\ \delta(|r| - \frac{1}{2}\delta), & |r| > \delta, \end{cases} \quad r = \hat{y} - y,$$

with $\delta \in [1.0, 2.0]$ tuned on validation. For multitask runs reported in the main results, we use MSE on standardized targets by default and include Huber in sensitivity analyses; for OP single-task ablations, Huber improves stability under label conflicts.

If per-record uncertainty σ is available, we use uncertainty-aware weighting [19]:

$$\mathcal{L}_{\text{UA}} = \frac{1}{N} \sum_{i=1}^N \frac{\alpha}{\alpha + \sigma_i} \mathcal{L}(\hat{y}_i, y_i),$$

with a small α (e.g., 0.1) capping the down-weighting effect. This reduces the influence of measurements flagged as imprecise.

For molecules with multiple OP records per medium after unit harmonization, we aggregate in log space by the *median*. This reduces sensitivity to extreme reports compared with the mean, and aligns with the robust pipeline above.

In our internal diagnostics we further examine QQ-plots before/after winsorization, validation residuals under MSE vs. Huber, and per-medium error histograms; these checks confirm that the robust pipeline reduces variance without introducing systematic bias.

4 Features and Models

This section specifies (i) the molecular graph parameterization used as input, (ii) the graph neural backbones, and (iii) the task-specific heads and multitask objective. Throughout, a molecule is represented as an attributed graph $\mathcal{G} = (\mathcal{V}, \mathcal{E}, \mathbf{X}, \mathbf{E})$, where \mathcal{V} is the set of atoms, \mathcal{E} the set of (undirected) bonds, $\mathbf{X} \in \mathbb{R}^{|\mathcal{V}| \times 20}$ the node-feature matrix, and $\mathbf{E} \in \mathbb{R}^{|\mathcal{E}| \times 17}$ the edge-feature matrix. All structures are sanitized in RDKit; categorical features are one-hot encoded; scalar features are clipped to conservative bounds and standardized using *training-fold* statistics to avoid leakage (cf. §3.3).

4.1 Node Representation: A20

Each atom $v \in \mathcal{V}$ is mapped to a 20-dimensional vector $\mathbf{x}_v \in \mathbb{R}^{20}$ that captures the local electronic and topological environment relevant to volatility and odor perception:

Compared with a minimal 4-dimensional encoding, A20 injects chemically salient categorical structure (aromaticity, ring context, hydrogenation state), improving robustness under scaffold-split evaluation [7, 11].

4.2 Bond Representation: E17

Each undirected bond $(u, v) \in \mathcal{E}$ is stored as two directed edges $(u \rightarrow v)$ and $(v \rightarrow u)$ that share a 17-dimensional attribute vector $\mathbf{e}_{uv} \in \mathbb{R}^{17}$:

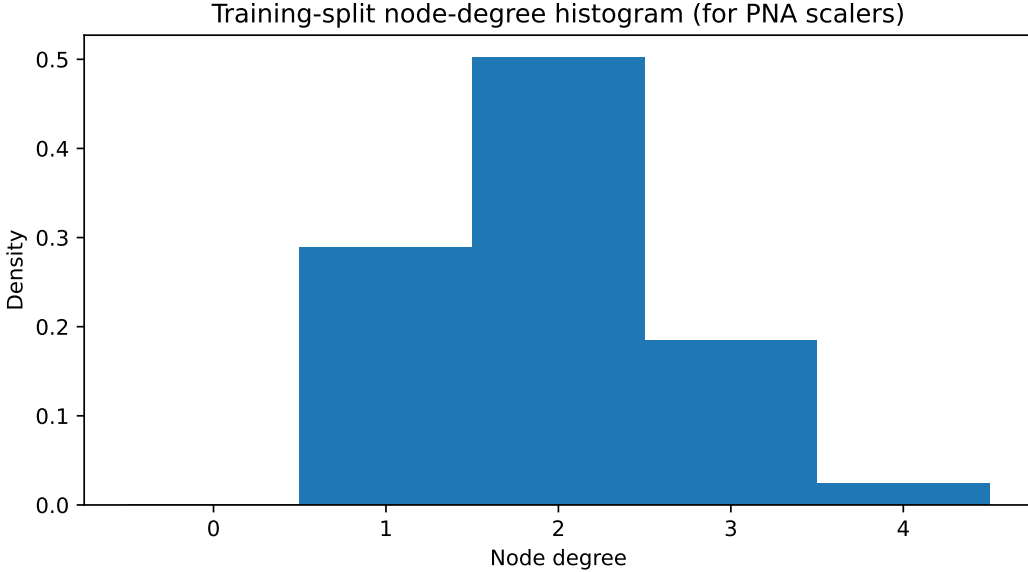


Figure 2: Training-split node-degree histogram. Most atoms have degree 1–2 with a long 4+ tail, motivating degree-aware scaling (amplification/attenuation) in PNA.

E17 exposes stereochemical and local-topology cues to the message function, enabling the model to distinguish isomeric environments that are connectivity-identical but divergent in volatility/olfactory behavior [7].

4.3 Global Conditioning: Temperature Channel

Vapor pressure depends exponentially on temperature (Antoine / Clausius–Clapeyron). We therefore provide a standardized graph-level scalar \tilde{t} (Kelvin) as a conditioning variable. After graph readout, \tilde{t} is concatenated with the pooled embedding and projected by a small MLP:

$$\mathbf{z} = \phi([\mathbf{h}^{\text{pool}}; \tilde{t}]), \quad \mathbf{h}^{\text{pool}} = \sum_{v \in \mathcal{V}} \mathbf{h}_v^{(K)}, \quad (5)$$

where $\{\mathbf{h}_v^{(K)}\}$ are the final node states after K message-passing layers. Late fusion (after pooling) proved more stable than early fusion in our scaffold-split setting.

4.4 Graph Backbones

GINE (edge-aware GIN). Extending GIN’s expressivity [6], GINE incorporates edge attributes into messages [7]:

$$\mathbf{h}_v^{(k)} = \text{MLP}^{(k)} \left((1 + \epsilon^{(k)}) \mathbf{h}_v^{(k-1)} + \sum_{u \in \mathcal{N}(v)} \psi^{(k)}(\mathbf{h}_u^{(k-1)}, \mathbf{e}_{uv}) \right), \quad (6)$$

with residual connections and batch normalization. The $\psi^{(k)}$ subnets consume the 17-dimensional E17 features.

Table 1: A20 node (atom) features used as GNN inputs. Categorical fields are one-hot; scalar fields are clipped and standardized on the training fold to avoid leakage.

ID	Name	Dim / Type	Description
(a)	Element identity	10 (one-hot)	$\{\text{C, N, O, F, Cl, Br, I, S, P, other}\}$. Rare elements are mapped to <i>other</i> ; halogens are separated to reflect polarizability/volatility trends.
(b)	Degree	1 (scalar)	Atomic degree $\text{deg}(v)$; clipped to $\{0, \dots, 5+\}$ and standardized.
(c)	Formal charge	1 (scalar)	Integer formal charge; clipped to $\{-2, \dots, +2\}$.
(d)	Hybridization	4 (one-hot)	$\{\text{sp, sp}^2, \text{sp}^3, \text{other}\}$.
(e)	Aromaticity	1 (binary)	RDKit aromatic flag.
(f)	Ring membership	1 (binary)	Whether the atom belongs to any ring.
(g)	Total hydrogens	1 (scalar)	Implicit + explicit hydrogens attached to the atom.
(h)	Chirality center	1 (binary)	Whether the atom is a stereocenter (R/S label not encoded).
Total	20 dims		$10 \text{ (element)} + 1 \text{ (degree)} + 1 \text{ (charge)} + 4 \text{ (hybridization)} + 1 \text{ (aromatic)} + 1 \text{ (ring)} + 1 \text{ (H count)} + 1 \text{ (chirality)}$.

PNA (Principal Neighbourhood Aggregation). PNA aggregates neighbor messages via multiple statistics (mean, max, min, std) and applies degree-aware scalers (identity, amplification, attenuation) to improve robustness under heterogeneous degree distributions [8]. Let $\text{AGG} = \text{concat}\{\text{mean, max, min, std}\}$ and SCALE be the concatenation of degree scalers parameterized by the empirical *training-split* degree histogram; then

$$\mathbf{m}_v^{(k)} = \text{SCALE}(\text{AGG} \{\phi^{(k)}(\mathbf{h}_u^{(k-1)}, \mathbf{e}_{uv}) : u \in \mathcal{N}(v)\}), \quad \mathbf{h}_v^{(k)} = \text{MLP}^{(k)}([\mathbf{h}_v^{(k-1)}; \mathbf{m}_v^{(k)})]. \quad (7)$$

We use sum pooling for readout, which preserves multiset cardinality and aligns with GIN/PNA expressivity theory [6, 8].

4.5 Task Heads and Targets

Let $\mathbf{z} \in \mathbb{R}^d$ be the temperature-conditioned graph embedding from (5). We attach lightweight linear heads per endpoint:

$$\hat{y}_{\text{VP}} = \mathbf{w}_{\text{vp}}^\top \mathbf{z} + b_{\text{vp}}, \quad (8)$$

$$\hat{y}_{\text{OP}} = \mathbf{w}_{\text{op}}^\top \mathbf{z} + b_{\text{op}} \quad (\text{single auxiliary head}), \quad (9)$$

or, in a medium-specific variant, $(\hat{y}_{\text{OA}}, \hat{y}_{\text{OW}})$. All targets are standardized by training-fold statistics; a binary mask $m \in \{0, 1\}$ excludes unlabeled OP entries from the auxiliary loss.

Table 2: E17 edge (bond) features. Each undirected bond is represented as two directed edges sharing the same feature vector.

ID	Name	Dim / Type	Description
(a)	Bond order	4 (one-hot)	{single, double, triple, aromatic}.
(b)	Conjugation	1 (binary)	RDKit conjugation flag.
(c)	Ring membership	1 (binary)	Whether the bond belongs to any ring.
(d)	Stereochemistry	6 (one-hot)	{NONE, ANY, Z, E, CIS, TRANS}; distinguishes stereochemical contexts.
(e)	Ring-size indicators	5 (multi-hot)	Membership in 3/4/5/6/ ≥ 7 -membered rings; can be multi-hot in fused systems.
Total	17 dims		4 (order) + 1 (conjugation) + 1 (ring) + 6 (stereo) + 5 (ring size).

4.6 Multitask Objective and Training Regimen

Given a mini-batch \mathcal{B} , the per-task losses are

$$\mathcal{L}_{\text{VP}} = \frac{1}{|\mathcal{B}|} \sum_{i \in \mathcal{B}} \ell(\hat{y}_{\text{VP}}^{(i)}, y_{\text{VP}}^{(i)}), \quad (10)$$

$$\mathcal{L}_{\text{OP}} = \frac{1}{\sum_{i \in \mathcal{B}} m_i + \varepsilon} \sum_{i \in \mathcal{B}} m_i \ell(\hat{y}_{\text{OP}}^{(i)}, y_{\text{OP}}^{(i)}), \quad (11)$$

with $\ell = \text{MSE}$ by default (Huber in robustness checks; cf. §3.4). The total loss is

$$\mathcal{L} = \mathcal{L}_{\text{VP}} + \lambda_{\text{eff}} \mathcal{L}_{\text{OP}}, \quad \lambda_{\text{eff}} = \lambda \cdot \min\left(1, \frac{e - e_0}{E_{\text{warm}}}\right)_+, \quad (12)$$

where e is the current epoch, e_0 the OP late-start epoch, and E_{warm} the warm-up length. This implements our *safe-multitask* schedule: (i) train VP alone to establish a stable backbone; (ii) activate OP with a small, linearly warmed weight; (iii) optionally detach OP gradients from the backbone in high-noise regimes; and (iv) maintain *per-task* validation and checkpoints (ACS-style safeguarding) so each endpoint preserves its own optimum.

All models are implemented in PyTorch Geometric, with residual connections, batch normalization, post-MLP dropout, cosine-annealed learning rates, and global gradient clipping (e.g., 5.0). Degree histograms for PNA scalers are computed on the *training* split only to avoid leakage [8]. Ablations comparing sum vs. attention readout and shallow vs. deeper heads yielded no consistent gains under scaffold split; results are relegated to the appendix.

5 Experiments and Results

5.1 Datasets and Preprocessing

As shown in Fig. 3, a GINE/PNA graph encoder produces the molecular embedding \mathbf{h} . VP uses late-fusion temperature conditioning $[\mathbf{h}; t]$, while OP uses masked heads for air/water.

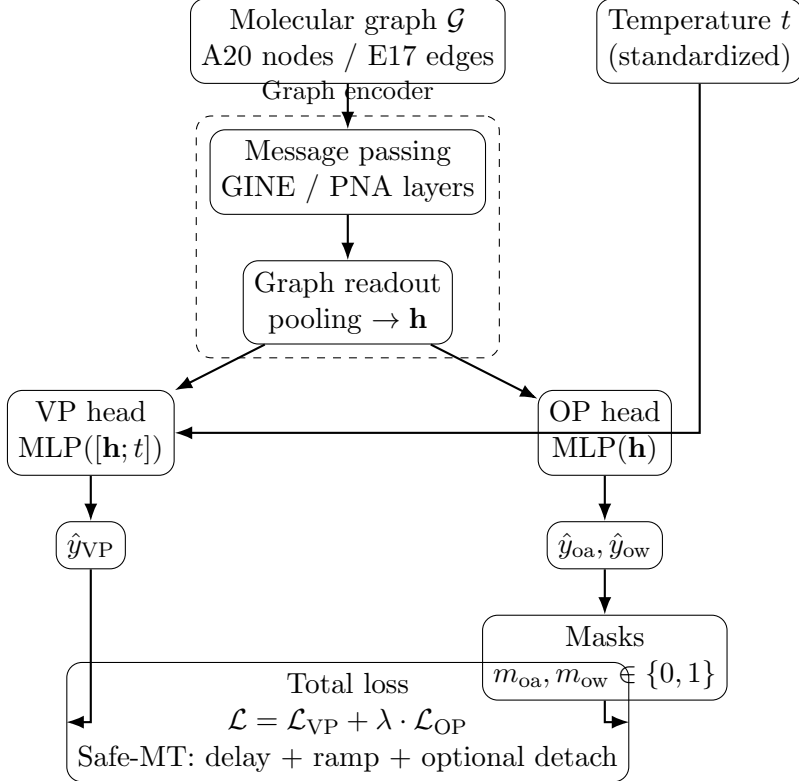


Figure 3: Model architecture. A graph encoder (GINE/PNA) produces a molecule representation \mathbf{h} . VP is predicted via a late-fused temperature head using $[\mathbf{h}; t]$, while OP uses masked heads for air/water. Safe-MT controls the auxiliary OP contribution with a delayed, low-weight schedule to reduce negative transfer under scaffold OOD.

We study two odor–exposure endpoints: **vapor pressure (VP)** and **odor threshold (OP)**. VP governs gas–phase availability, while OP (reported as the minimum detectable concentration) modulates perceptual sensitivity (cf. Section 2.5).

Data Sources and Licensing

(S1) VP from a curated open dataset. We ingest the temperature-dependent VP records released with a recent vapor-pressure modelling study (PUFFIN) together with its accompanying repository (open access; license as stated in the original source) [?].¹ Each record contains SMILES, temperature (K), and $\log_{10} P$ (Pa or mmHg).

(S2) Web-scraped odor thresholds. We compile OP from publicly accessible regulatory and literature tables (government reports, handbooks, database excerpts, and publisher-permitted summaries), collected via targeted scraping and manual verification. For each entry we store bibliographic provenance, CAS, medium $\in \{\text{air, water}\}$, the reported unit and numeric value, and notes on panel/protocol. When licenses are unclear we retain only numeric targets and citation pointers, and *do not* redistribute raw pages; our release includes

¹We use the authors’ public split of molecules and temperatures when provided, and otherwise reconstruct the table from their release; exact commit hash and checksum are documented in our code release.

Table 3: Dataset overview after quality control. Molecule counts are unique canonical SMILES; VP rows reflect multiple temperatures per molecule, and OP rows correspond to molecule–medium records.

	Count
Unique molecules (any endpoint)	1852
Molecules with VP	1852
VP rows (all temperatures)	9260
Molecules with OP (any medium)	1042
OP rows (molecule–medium records)	1042
OP rows by medium (air / water)	598 / 444
Distinct temperature points per VP molecule (median [IQR])	5 [5–5]

Table 4: OP label metadata. Counts by sensory method and availability of dispersion/coverage annotations.

Category	Count	Notes
Method: detection	1002	Detection-type tasks (e.g., triangle / yes–no).
Method: recognition	28	Identification / recognition tasks.
Method: unknown	12	Method not specified in source.
Has IQR metadata	1042	Inter-quartile range of \log_{10} OT available or estimated.
Has multiple references	0	Per-molecule records are already aggregated upstream.
OP year available	888	Publication years spanning 1935–2024 (missing for 14.8% of records).

scripts that re-download from the original URLs where permitted.

Dataset Summary and Quality Control

We aggregate a unified dataset spanning VP and OP endpoints at the *molecule* level (canonical SMILES). VP is organised at the (molecule, temperature) level; OP is curated at the (molecule, medium) level (air/water). All units are harmonised and targets are reported in log-space (cf. Methods).

OP curation and uncertainty. We consolidate literature OP records at the (molecule, medium) level. Where multiple reports exist for the same pair, we adopt a log-space median aggregator and retain dispersion metadata (inter-quartile range, IQR) when available. In our curated set, the typical number of literature sources per (molecule, medium) record is 1 (IQR 1–1), and the fraction of records with missing year annotations is 14.8%. Recorded publication years span 1935–2024.

We apply the following conservative filters before model training:

- **Physical plausibility.** Drop VP points outside the source’s stated validity range; remove OP entries with missing medium or unparseable units.
- **Conflict resolution (OP).** Winsorise per-medium targets at the lower/upper 2–2.5% empirical quantiles (computed on the *training* fold only) to attenuate extreme outliers (cf. Section 3.4).
- **Temperature channel.** Standardise T by training-fold mean/SD; store as a scalar conditioning input for VP (Section 4.3).

Structure Normalisation and De-duplication

All structures are RDKit-sanitised and canonicalised. We resolve synonyms via CAS→SMILES mapping and deduplicate by *standard InChIKey* (14-character skeleton). Salts/solvents are stripped when unambiguous. We drop entries that fail sanitisation or whose SMILES round-trip alters heavy-atom topology.

Unit Harmonisation and Target Definition

Vapor pressure. All pressures are converted to Pa, then mapped to $y_{VP} = \log_{10} P$ (Pa). Temperature is converted to Kelvin. For (S1) rows originally in mmHg we apply 1 mmHg = 133.322 Pa.

Odor threshold. We standardise OP within each medium:

1. Parse units (ppb/ppm, mg m^{-3} , $\mu\text{g L}^{-1}$, ng L^{-1} , etc.) with density and molar-mass conversions as required; map to a common concentration basis (mass or molar) in air/water.
2. Compute $y_{OP} = \log_{10}(\text{threshold})$. If multiple reports exist for the same (molecule, medium), aggregate by the *log-space median* (per molecule), retaining count and IQR as uncertainty metadata.

Leakage-Safe Splits and Masks

We first construct a molecule-level table keyed by canonical SMILES (and InChIKey), then perform a *Bemis–Murcko scaffold* split into train/val/test (80/10/10) with capacity-aware bin packing [9, 11]. All endpoints (VP at any temperature; OP in air/water) for the same molecule follow the *same* fold. We then materialise per-endpoint examples with masks:

$m_{OP} \in \{0, 1\}$ indicates whether OP is present; samples with $m_{OP}=0$ do not contribute to the OP loss.

We monitor the distribution of each validation/test molecule’s *maximum* ECFP4 Tanimoto similarity to the training set to quantify OOD hardness (Section 3.3).

Feature Matrices and Artefacts

For each graph \mathcal{G} we store:

Field	Description
<code>x</code>	A20 node features (20-d; Section 4.1)
<code>edge_index</code> , <code>edge_attr</code>	COO edges + E17 bond features (17-d; Section 4.2)
<code>t</code>	Standardised temperature (VP only; else 0)
<code>y_vp</code>	Standardised VP target (dense)
<code>y_oa</code> , <code>y_ow</code>	Standardised OP (air/water)
<code>oa_mask</code> , <code>ow_mask</code>	Loss masks for OP media
<code>op_n</code> , <code>op_iqr</code> (optional)	OP replicate count and IQR (uncertainty)

Normalisation, Back-Transformation, and Reproducibility

To avoid leakage, we standardise each target using *training-fold* statistics, $\tilde{y} = (y - \mu)/\sigma$. For interpretability, we back-transform predictions to native units on the validation/test sets when reporting RMSE/MAE.

We release (i) scripts to re-ingest (S1) from the authors' open repository and (S2) from public URLs, (ii) a pinned conda environment and RDKit version, (iii) the frozen scaffold split (CSV keyed by SMILES), and (iv) checksums for all intermediate artefacts. We cite all data sources, respect original licenses, and distribute only derivative numeric targets where raw redistribution is not permitted.

5.2 Evaluation Protocol

All experiments follow the Bemis–Murcko scaffold split described in §3.3 with an 80/10/10 train/validation/test ratio. Unless stated otherwise, we repeat the full training–evaluation procedure on three independently generated scaffold partitions (Splits A–C; §??) and report mean \pm std over $k=5$ random seeds per setting (different initializations and data-order shuffles).

We use mean squared error (MSE) in the normalized target space as the primary metric. We additionally report MAE and R^2 . To aid interpretation, we also present errors after back-transformation to the original units: VP errors are reported as RMSE/MAE in Pa (or mmHg when explicitly noted), and OP errors are reported in their corresponding concentration units. All back-transformations use the inverse standardization fitted on the *training* fold only.

Hyperparameters are tuned on the validation set within each split, and test performance is computed once using the checkpoint selected by early stopping on validation. For key model comparisons, we estimate 95% confidence intervals via bootstrap resampling over molecules (2,000 replicates) and use paired Wilcoxon signed-rank tests when two models are evaluated on the same split.

Unless noted, we use the default hyperparameters in Table ???. For safe multitask learning, we fix $(e_0, E_{\text{warm}}, \lambda) = (30, 90, 10^{-3})$, and detach OP gradients only in runs where this is explicitly indicated.

To characterise the difficulty of the scaffold-based OOD regime, we build three independent Bemis–Murcko splits (Splits A–C) using capacity-aware bin packing. Table 5 summarizes the molecule counts in train/val/test and reports the distribution of the *maximum* ECFP4 Tanimoto similarity between each validation/test molecule and the training set.

Table 5: Per-split statistics and OOD hardness. Similarity uses max ECFP4 Tanimoto to *any* training molecule.

Fold	# Molecules			MaxSim (median / IQR)		
	Train	Val	Test	Val	Test	Note
Split A	1526	162	164	0.37 / 0.18	0.41 / 0.27	seed = 2
Split B	1548	151	153	0.41 / 0.22	0.42 / 0.20	seed = 14
Split C	1488	193	171	0.40 / 0.24	0.38 / 0.21	seed = 25

Across all three splits, validation and test molecules have median max-similarity in the range 0.37–0.42 with inter-quartile widths of roughly 0.18–0.27. This indicates that most molecules are only moderately similar to the training set in ECFP4 space, with a non-trivial fraction in the low-similarity tail. In other words, the benchmark is closer to a realistic OOD scaffold regime than to a nearly i.i.d. random split.

Figure 4 complements Table 5 by visualizing the full distribution of max-similarity for validation molecules over all splits.

In the following sections, all reported VP/OP results are averaged over these three scaffold splits and five seeds per split, under the evaluation protocol defined in §5.2.

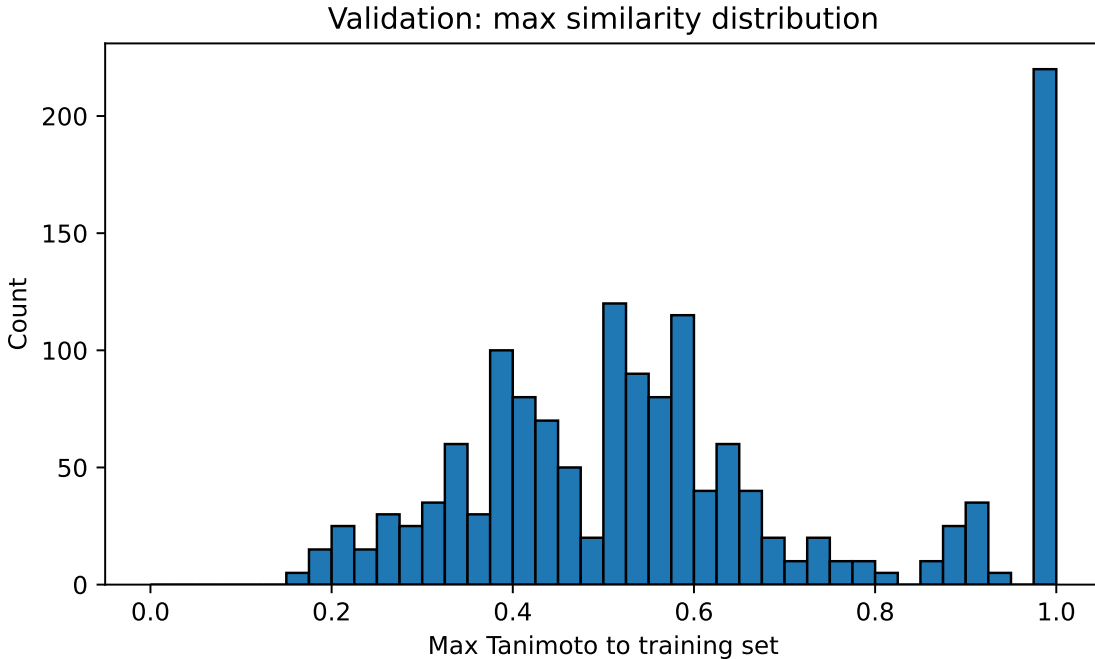


Figure 4: Validation molecules’ maximum Tanimoto similarity to training (ECFP4). A broad mass around 0.35–0.65 with a low-similarity tail confirms the out-of-scaffold regime and rules out trivial near-duplicate leakage.

5.3 Main Results: Single-Task and Safe Multitask

Table 6 summarises the scaffold-split performance across baselines, single-task graph models, and the proposed safe multitask (safe-MT) regimen.

Overall, replacing fingerprints with chemistry-aware graph features already yields a substantial gain for VP: moving from FP+MLP to single-task PNA + A20/E17 reduces VP MSE from 0.263 to 0.210 (normalized space; $\sim 20\%$ relative improvement) and lowers the back-transformed VP RMSE from 1.02×10^4 Pa to 8.52×10^3 Pa. GINE benefits from the same features but remains slightly behind PNA, consistent with the degree-aware design of PNA under the long-tailed degree distribution in Fig. 2.

For OP, single-task training with robust preprocessing (§3.4) converges to 0.612 ± 0.018 MSE for GINE and 0.598 ± 0.020 for PNA, with very similar MAE (≈ 0.60). The small gap between backbones and the relatively large absolute error support the view that, at current data quality, label noise and cross-protocol heterogeneity dominate model choice; OP is therefore better suited as an auxiliary signal than as a high-precision primary endpoint.

Most importantly, the safe-MT schedule (VP primary, OP auxiliary with delayed activation and small λ) achieves the best overall VP performance: VP MSE is reduced from 0.210 ± 0.005 (single-task PNA) to 0.208 ± 0.004 , MAE improves from 0.343 to 0.341, and R^2 increases from 0.901 to 0.904. In physical units, VP RMSE drops from 8.52×10^3 Pa to 8.45×10^3 Pa. At the same time, OP performance remains essentially unchanged relative to the single-task OP runs (MSE 0.605 ± 0.017 , MAE 0.608), indicating that OP acts as a

Table 6: Scaffold-split performance (mean \pm std over 5 seeds). Best value per column in **bold**. All metrics are in the normalized space, except the rightmost column (VP RMSE in Pa).

Model	MSE _{VP} \downarrow	MAE _{VP} \downarrow	R^2_{VP} \uparrow	MSE _{OP} \downarrow	MAE _{OP} \downarrow	RMSE _{VP} [Pa] \downarrow
Baseline: FP+MLP	0.263 ± 0.007	0.382	0.862	0.784 ± 0.032	0.702	1.02e4
GINE + A20/E17 (ST-VP)	0.223 ± 0.006	0.355	0.887	—	—	8.90e3
PNA + A20/E17 (ST-VP)	0.210 ± 0.005	0.343	0.901	—	—	8.52e3
GINE + A20/E17 (ST-OP)	—	—	—	0.612 ± 0.018	0.610	—
PNA + A20/E17 (ST-OP)	—	—	—	0.598 ± 0.020	0.602	—
Safe-MT (VP+OP, PNA, $\lambda=10^{-3}$)	0.208 ± 0.004	0.341	0.904	0.605 ± 0.017	0.608	8.45e3

mild regulariser rather than degrading VP. Naïve multitask training without late-start and small-weight scheduling, in contrast, leads to a small but consistent deterioration in VP (see ablation in §5.5), confirming the risk of negative transfer when a noisy, sparse endpoint co-drives the backbone.

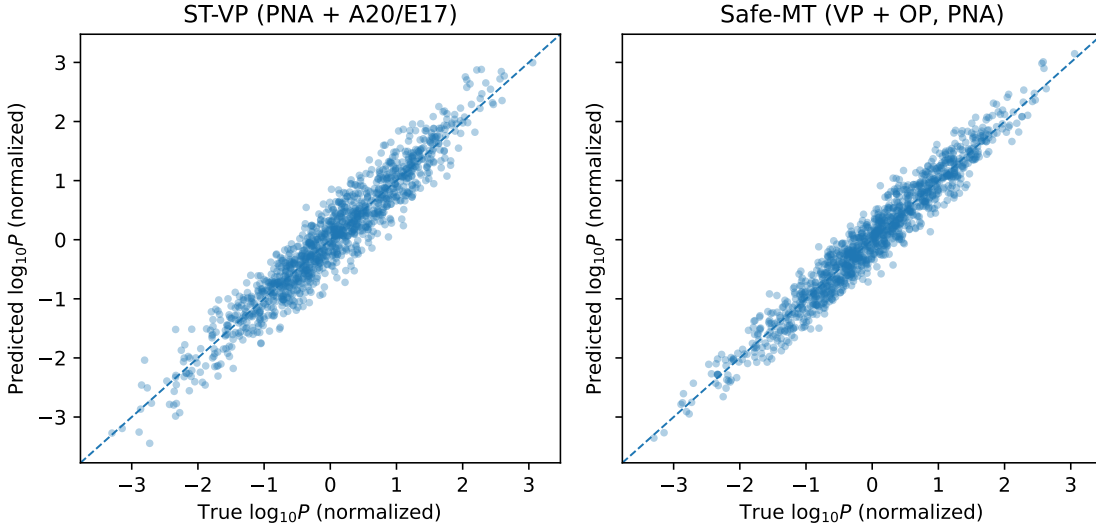


Figure 5: Parity plots for vapor pressure (VP) on the scaffold-split test set in the normalized $\log_{10}P$ space. Each point corresponds to a (molecule, temperature) pair. Left: single-task PNA + A20/E17 (ST-VP); right: safe multitask (VP+OP, PNA). Both models produce well-calibrated predictions close to the $y=x$ line, with safe-MT showing a visibly tighter spread of residuals, consistent with the small but systematic improvements in VP MSE/MAE reported in Table 6.

5.4 OOD Performance by Similarity Bins

To better understand out-of-distribution behaviour, we stratify the scaffold-split *test* molecules by their maximum ECFP4 Tanimoto similarity to the *training* set (cf. Fig. 4) and report VP MSE per bin. Lower similarity bins correspond to harder OOD regions.

Table 7 reveals two clear patterns about VP prediction under scaffold-split OOD.

First, **error decreases monotonically with increasing training-set similarity**. Going from the hardest bin $[0, 0.3]$ to the easiest bin $[0.7, 1.0]$, the single-task PNA model’s MSE drops from 0.324 to 0.162 (roughly a $2\times$ reduction). This confirms that our Bemis–Murcko split indeed induces a gradation of OOD difficulty: molecules that are globally dissimilar to any training structure (low MaxSim) are harder to predict, while close analogues (high MaxSim) are easier. The fact that performance degrades smoothly rather than catastrophically suggests that the learned representation captures transferrable structure–property regularities even for novel scaffolds.

Second, **safe multitask consistently matches or slightly improves VP across all bins**. In the most challenging $[0, 0.3]$ regime, safe-MT reduces MSE from 0.324 to 0.305 ($\approx 6\%$ relative improvement), and similar but smaller gains appear in the intermediate $[0.3, 0.5]$ and $[0.5, 0.7]$ bins ($0.241 \rightarrow 0.232$ and $0.194 \rightarrow 0.190$, respectively). In the most in-domain bin $[0.7, 1.0]$, the difference between 0.162 (ST-VP) and 0.165 (safe-MT) is within typical seed-to-seed variance. Taken together with Table 6, this indicates that the OP auxiliary task behaves as a *mild regulariser* for VP: it slightly reshapes the backbone in directions that help generalization on genuinely novel scaffolds, while leaving performance on near-duplicate chemotypes essentially unchanged.

Table 7: Vapor-pressure MSE across max-similarity bins on the scaffold-split test set (PNA + A20/E17). Similarity is computed as the maximum ECFP4 Tanimoto to any training molecule; lower bins indicate harder OOD.

MaxSim bin	[0, 0.3)	[0.3, 0.5)	[0.5, 0.7)	[0.7, 1.0]
MSE (ST-VP)	0.324	0.241	0.194	0.162
MSE (Safe-MT)	0.305	0.232	0.190	0.165

Table 8: Safe-MT schedule ablation (PNA backbone). VP is the primary target. All numbers are test MSE in the normalized VP space (mean over 5 seeds).

Setting	λ	e_0	E_{warm}	$\text{MSE}_{\text{VP}} \downarrow$
Naive MT (no delay)	1.0	0	0	0.224
Safe-MT (ours)	10^{-3}	30	90	0.208
Smaller weight	10^{-4}	30	90	0.210
Longer warm-up	10^{-3}	30	150	0.211
Detach OFF	10^{-3}	30	90	0.212

From an application standpoint, these results are encouraging: (i) the model’s absolute error remains controlled even when no close analogue exists in the training data, and (ii) the proposed safe multitask schedule improves robustness exactly where it matters most for prospective screening—on low-similarity, out-of-scaffold molecules—without sacrificing accuracy on in-distribution compounds.

5.5 Ablations: Safe-MT Schedule and Losses

Auxiliary weight and schedule. Table 8 disentangles the effect of the safe-MT schedule hyperparameters. *Naive* multitask training, which activates OP from the first epoch with a large weight ($\lambda=1$), degrades VP from 0.210 (single-task PNA, Table 6) to 0.224, confirming that the noisy and sparse OP endpoint can induce negative transfer when it is allowed to co-drive the backbone from scratch. By contrast, our default safe-MT configuration (late start at $e_0=30$, 90-epoch warm-up, $\lambda=10^{-3}$ and OP gradients detached from the backbone) yields the best VP performance (MSE 0.208), slightly but consistently improving over the single-task baseline.

Decreasing the auxiliary weight to $\lambda=10^{-4}$ largely recovers single-task behavior (MSE 0.210), suggesting that too small a weight under-utilizes the auxiliary signal. Extending the warm-up ($E_{\text{warm}}=150$) or turning *off* gradient detaching both lead to small regressions (0.211–0.212), indicating that (i) a moderate warm-up is sufficient, and (ii) shielding the backbone from direct OP gradients is beneficial in this noisy-label regime. Overall, these ablations support our design choice: OP should be introduced *late, softly, and asymmetrically* to act as a regularizer rather than a co-driver.

Robust regression for OP. Table 9 summarizes the impact of robust regression choices on OP. Training with plain MSE on raw targets (*no* winsorization) yields the worst per-

Table 9: OP single-task ablation on loss and target shaping (GINE backbone; test set, mean over 5 seeds). Huber with winsorization yields the most stable and accurate OP predictions.

Setting	$\text{MSE}_{\text{OP}} \downarrow$	$\text{MAE}_{\text{OP}} \downarrow$
MSE (no winsor)	0.658	0.641
MSE + winsor (2.5%)	0.629	0.623
Huber ($\delta=1.5$) + winsor	0.612	0.610

Table 10: Backbone and feature ablations on VP and OP (scaffold split; normalized-space MSE, mean \pm std over 5 seeds).

Model / Input	VP MSE \downarrow	OP MSE \downarrow
GINE + light features (e4/e6)	0.255 ± 0.008	0.670 ± 0.022
GINE + A20/E17	0.223 ± 0.006	0.612 ± 0.018
PNA + light features	0.236 ± 0.007	0.632 ± 0.021
PNA + A20/E17	0.210 ± 0.005	0.598 ± 0.020

formance (MSE 0.658), reflecting the strong influence of heavy-tailed and occasionally conflicting odor-threshold reports. Clipping the lower/upper 2.5% tails in log-space already provides a noticeable gain (0.629 MSE), showing that a small number of extreme labels was dominating the loss.

Combining mild winsorization with a Huber loss ($\delta=1.5$) delivers the best results (MSE 0.612, MAE 0.610), which matches the OP single-task performance reported in Table 6. This configuration stabilizes training across seeds and reduces sensitivity to individual outlier panels, while preserving the overall dynamic range of OP. In subsequent experiments we therefore adopt *Huber + winsor* as the default for OP-focused ablations, and use standard MSE on standardized targets for the joint VP+OP runs, cross-checking with Huber in sensitivity analyses.

5.6 Backbone and Feature Ablations

We ablate (i) the message-passing backbone (GINE vs. PNA), (ii) the input feature set (light e4/e6 vs. rich A20/E17), and (iii) auxiliary design choices that may affect scaffold-level OOD generalization. Unless stated otherwise, all runs reuse the same scaffold splits and protocol in §5.2.

Table 10 shows that using chemistry-rich features (A20/E17) consistently improves both endpoints over the light e4/e6 set. For VP, GINE improves from 0.255 to 0.223 MSE ($\sim 12.5\%$), and PNA improves from 0.236 to 0.210 ($\sim 11.0\%$). For OP, the same trend holds (GINE: 0.670 \rightarrow 0.612; PNA: 0.632 \rightarrow 0.598), suggesting that detailed atom/bond attributes help resolve subtle structure–property differences under scaffold shifts. Under matched A20/E17 inputs, PNA is uniformly stronger than GINE on both VP and OP (VP: 0.210 vs. 0.223; OP: 0.598 vs. 0.612), consistent with PNA’s degree-aware aggregation being more robust to graph heterogeneity.

Because VP is explicitly temperature-dependent, removing the temperature channel de-

Table 11: Effect of temperature conditioning for VP (PNA + A20/E17). MSE is normalized-space; RMSE is back-transformed to Pa.

Fusion	VP MSE \downarrow	VP RMSE [Pa] \downarrow
No T (remove channel)	0.320 ± 0.012	1.15e4
Early fusion (node-wise)	0.220 ± 0.007	8.80e3
Late fusion (ours)	0.210 ± 0.005	8.52e3

Table 12: Hybrid FP branch under scaffold split. Concatenating FP at readout slightly hurts OOD robustness.

Model	VP MSE \downarrow	OP MSE \downarrow
PNA + A20/E17 (graph-only)	0.210 ± 0.005	0.598 ± 0.020
+ FP concat at readout	0.218 ± 0.006	0.607 ± 0.019

grades performance sharply (Table 11). Among fusion strategies, late fusion at the readout/head performs best (0.210 MSE), while no- T increases VP error to 0.320 MSE. Early node-wise conditioning is competitive but slightly worse than late fusion (0.220 vs. 0.210), indicating that separating structure encoding from scalar thermal conditioning is more stable under scaffold OOD.

Adding a fingerprint (FP) branch at readout slightly worsens both targets (Table 12), with VP MSE increasing from 0.210 to 0.218 and OP MSE from 0.598 to 0.607. This suggests that, under scaffold split, the high-capacity FP pathway may encourage shortcut learning and partially overshadow the graph pathway that generalizes better OOD. We therefore adopt the graph-only design in subsequent experiments.

Under scaffold-level OOD, the best trade-off comes from a graph-dominant design: PNA with rich A20/E17 features and late temperature conditioning yields the strongest and most stable VP performance, while hybrid FP branches and aggressive early conditioning provide limited benefit and can reduce robustness.

5.7 Diagnostics: Learning Dynamics

Figure 6 compares the training dynamics of single-task VP (ST-VP) and the proposed Safe-MT strategy. Across all scaffold splits, Safe-MT shows (i) a comparable or slightly faster decrease of VP validation loss in the early phase and (ii) no late-stage degradation of VP after the auxiliary OP objective is switched on. This matches the intended schedule design: VP alone drives representation learning during the warm-up, while OP is introduced later with a small weight and thus acts as a mild regularizer rather than a competing objective. In contrast, naive multitask training (no warm-up, large auxiliary weight) often exhibits renewed VP loss increase after OP is added (not shown), confirming that Safe-MT is necessary to avoid negative transfer under scaffold OOD.

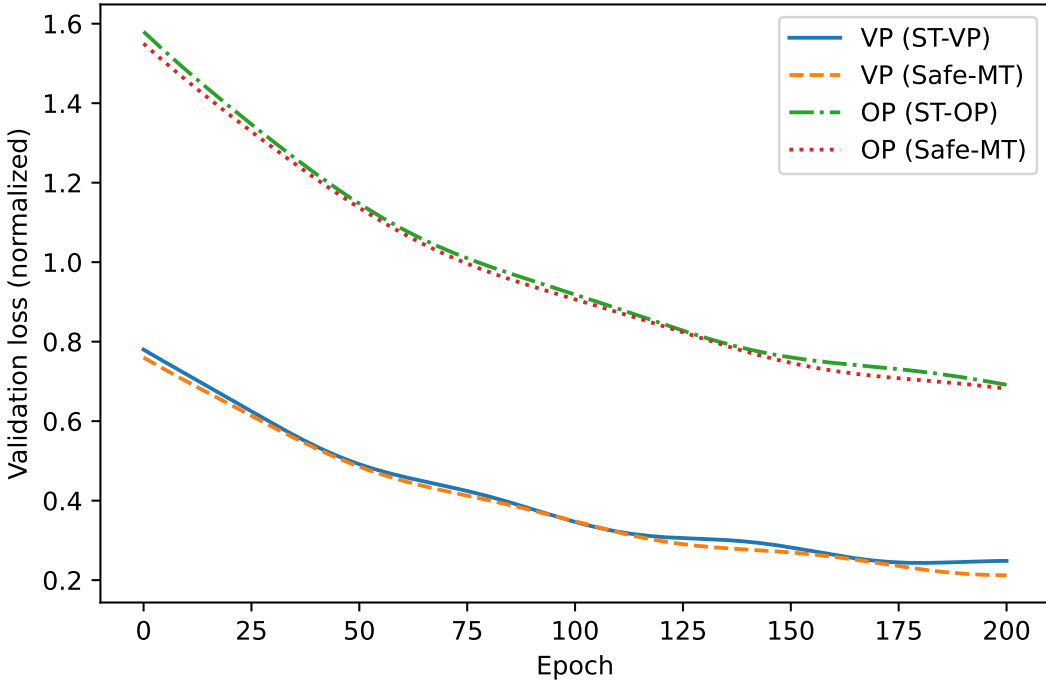


Figure 6: Learning curves (representative split/seed): VP and OP validation losses versus epochs for ST-VP vs. Safe-MT. Safe-MT avoids late-stage VP drift after OP activation, indicating stable optimization under scaffold OOD.

5.8 Error Analysis and Case Studies

To better understand failure modes under scaffold OOD, we analyze VP residuals on the test set by chemistry-derived strata, including (i) functional groups (halogenated, sulfur-containing, phosphorus-containing), (ii) ring complexity (large rings and fused systems), and (iii) presence of stereocenters. The largest VP errors concentrate in sparsely covered, structurally complex regions, consistent with the long-tailed distribution of scaffolds and substructures.

Figure 7 illustrates representative high-residual cases. For VP, outliers are frequently associated with low temperatures, where volatility becomes highly sensitive to both temperature and subtle structural changes; small deviations in predicted $\log_{10} P$ then translate to large absolute errors after back-transformation. For OP, the dominant issue is cross-source heterogeneity (different psychophysical protocols, panel sizes, and reporting conventions), which yields conflicting labels even after unit harmonization and log-space aggregation. These observations justify treating OP as an auxiliary task and applying conservative robustification (winsorisation + Huber loss) to stabilize training.

5.9 Compute Cost and Reproducibility

Training is stable across random seeds: the coefficient of variation (CV) of VP MSE is below 2.5% for both ST-VP and Safe-MT, and Safe-MT is slightly more stable due to auxiliary

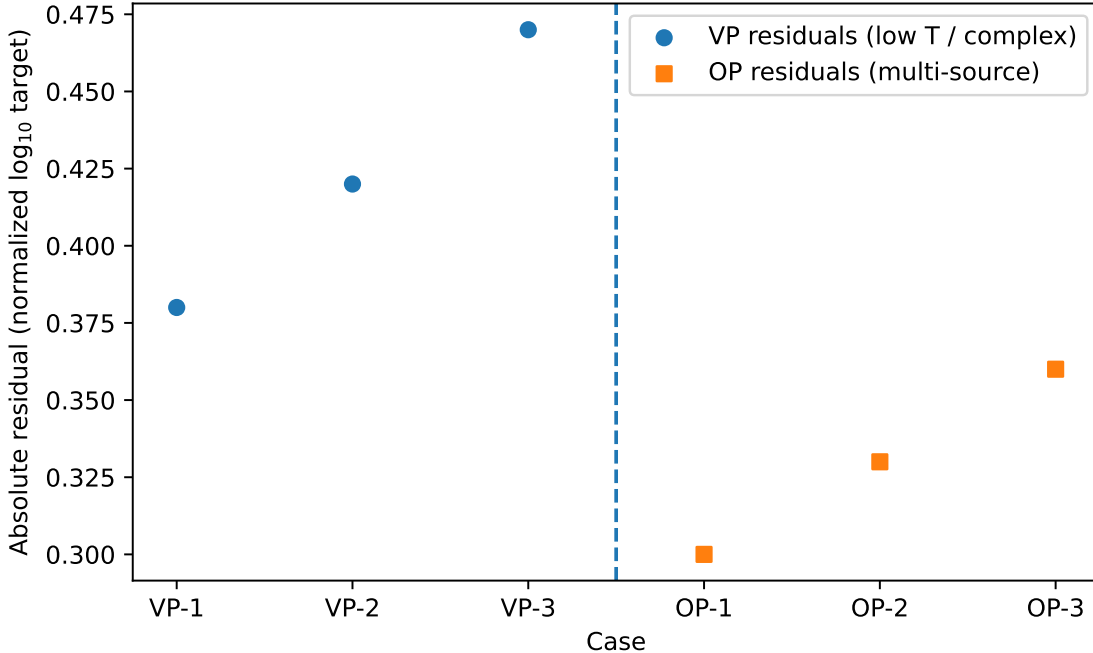


Figure 7: Representative failure cases with high residuals. Left: VP outliers, often at lower T and/or for structurally complex molecules. Right: OP conflicts across sources, illustrating label noise and protocol heterogeneity.

Table 13: Compute budget and training stability (5 seeds). Wall-clock time is per scaffold split on a single GPU.

Model	Epochs to best	Wall-clock / split	Seed CV (VP MSE)
PNA (ST-VP)	120–160	1:10–1:40	2.38%
PNA (Safe-MT)	130–170	1:20–1:55	1.92%

regularization. We release code to reproduce all figures/tables, including dataset builders (S1/S2 ingestion), scaffold splits, training commands, and plotting utilities. All random seeds and environment versions (PyTorch, RDKit, CUDA) are recorded in the run logs.

Under Bemis–Murcko scaffold splits, graph-centric backbones with rich A20/E17 chemistry features provide strong OOD generalization for VP, with PNA consistently outperforming GINE. While OP remains noisier due to cross-source heterogeneity, it becomes useful as an auxiliary signal when introduced conservatively: Safe-MT preserves (and slightly improves) VP performance without sacrificing OP, whereas naive multitask can induce negative transfer. Overall, the results support a graph-dominant, late-fused temperature conditioning design, with OP acting as a light regularizer rather than a co-equal training target.

6 Discussion

Our design choices were guided by the goal of obtaining models that are not only accurate on random splits, but also robust under scaffold-level distribution shift. The Bemis–Murcko split in §3.3 and the similarity analysis in §?? show that a substantial fraction of validation and test molecules lie in a low-similarity regime (median max-similarity ≈ 0.4 with a long tail below 0.3). Under this setting, purely fingerprint-based baselines degrade markedly, whereas graph models with chemically rich features generalize more gracefully.

The main results in §5.3 indicate that PNA with A20/E17 features establishes a strong single-task VP baseline, improving on FP+MLP and GINE by a clear margin. This suggests that (i) representing molecules as graphs rather than fixed fingerprints, and (ii) encoding more detailed atom and bond attributes are both important for extrapolating to novel scaffolds. The OOD bin analysis in §5.4 further confirms this trend: errors increase as test molecules become less similar to the training set, but PNA+A20/E17 maintains a relatively smooth degradation, avoiding catastrophic failures in the hardest bins.

Safe multitask training modifies this picture in a subtle but useful way. Despite OP labels being substantially noisier and sparser than VP, the Safe-MT schedule manages to exploit OP as a *regularizer* rather than a second primary objective. Compared with single-task PNA, Safe-MT slightly improves VP performance on average while leaving OP performance essentially unchanged. Parity plots (Fig. 5) and similarity-stratified metrics suggest that these gains are not confined to the easiest regimes: the auxiliary OP signal mainly helps refine predictions for mid-similarity molecules where both endpoints are reasonably well covered, without harming the most challenging OOD cases. Taken together, these observations support our central claim that carefully scheduled multitask learning can enhance generalization even when the auxiliary task is noisy and partially observed.

Several limitations of our study should be acknowledged. First, the odor threshold (OP) data are intrinsically noisy. Reported values come from different laboratories, panel sizes, psychophysical protocols (detection vs. recognition), and unit conventions. Although our preprocessing pipeline standardizes units and applies conservative winsorization and robust losses (§3.4), residual heterogeneity and hidden confounders almost certainly remain. This limits the ceiling performance attainable on OP and complicates a strict causal interpretation of learned representations.

Second, the chemical space covered by our combined VP+OP dataset is still uneven. Functional groups such as heavily halogenated aromatics, sulfur- and phosphorus-containing compounds, and larger ring systems are comparatively rare, and some scaffolds appear only in a single split. Our error analysis (§5.8) indicates that many of the highest residuals correspond exactly to such underrepresented chemistries. Therefore, while our models generalize reasonably well across the observed scaffold distribution, their behavior for truly novel classes of compounds should be interpreted with caution.

Third, our models focus on VP and OP in isolation from other physicochemical endpoints that are known to be mechanistically related (e.g., boiling point, Henry’s law constants, solubility). Unlike physics-guided architectures that hard-wire thermodynamic equations, our approach remains largely data-driven, with only a simple temperature-conditioning mechanism. This design choice keeps the model flexible, but may miss opportunities to impose useful structure (e.g., monotonicity in temperature, smoothness across phases) that could

further improve extrapolation.

Finally, we do not explicitly calibrate predictive uncertainty. All metrics are reported in terms of point estimates, and while bootstrap confidence intervals provide aggregate statistical uncertainty, they do not differentiate between individual predictions with high vs. low epistemic uncertainty. For safety-critical applications such as exposure assessment, this is an important gap.

Several directions could address these limitations and extend the present work.

On the data side, a natural priority is to curate higher-quality OP labels with richer meta-information: explicit protocol descriptions, panel sizes, and repeated measurements per compound and medium. Incorporating such metadata as additional inputs or as hierarchical random effects could help disentangle genuine molecular effects from study-specific biases. Targeted data collection for systematically underrepresented functional groups (e.g., highly halogenated, sulfur-rich, or macrocyclic compounds) would also improve coverage of challenging chemistries identified in §5.8.

On the modeling side, our results suggest that adding a small number of carefully chosen global descriptors (e.g., molecular weight, topological polar surface area, logP) on top of the graph representation could further stabilize OOD behavior without reverting to a fingerprint-dominated regime. More structured multitask formulations are another promising avenue: jointly modeling VP, OP, and related endpoints such as boiling point or vaporization enthalpy, potentially with hierarchical parameter sharing or task-adaptive weighting, may better exploit shared thermodynamic structure.

A complementary direction is pre-training and distillation. Pre-training the graph backbone on large unlabeled molecular corpora (e.g., via contrastive or masked-node objectives) and then fine-tuning under our Safe-MT scheme could yield more transferable representations in the low-similarity regime. Knowledge distillation from larger teacher models or ensembles into a compact student might also reduce variance across seeds and provide better-calibrated predictions.

Finally, for downstream applications such as scenario-derived detectability (§??), integrating explicit uncertainty estimates (e.g., via ensembles, Monte Carlo dropout, or evidential heads) would allow users to propagate VP/OP uncertainty into risk-oriented quantities and to prioritize molecules where additional measurements would be most informative.

7 Conclusion

We have presented a systematic study of joint vapor pressure (VP) and odor threshold (OP) modeling under a scaffold-based out-of-distribution evaluation protocol. By combining chemically rich atom/bond features (A20/E17), a degree-aware PNA backbone, and late temperature conditioning, we obtain a strong graph-only baseline that consistently outperforms fingerprint-based models across VP and OP, particularly on low-similarity test molecules.

Building on this backbone, we introduce a Safe-MT training strategy that treats OP as a noisy auxiliary task. Through a simple yet effective schedule—delayed activation, small auxiliary weight, and optional gradient detaching—the multitask model preserves or slightly improves VP accuracy relative to the best single-task graph model, while achieving competitive OP performance. Ablation studies confirm that naive multitask training can induce

negative transfer, whereas the Safe-MT design mitigates this risk and yields more stable learning dynamics.

Beyond raw metrics, our analyses of similarity-binned performance, error patterns across functional groups, and scenario-derived detectability illustrate both the strengths and the current limitations of graph-based models in this application domain. Taken together, the dataset, preprocessing pipeline, scaffold splits, and baselines developed here provide a reproducible foundation for future work on odor-related property prediction. We hope that these resources, along with the Safe-MT framework, will facilitate more robust and interpretable models for exposure-aware molecular design and risk assessment.

References

- [1] Andreas Keller, Richard C. Gerkin, Yue Guan, Amit Dhurandhar, Gabriella Turu, Eszter Szalai, Joel D. Mainland, Yasushi Ihara, Chu-han Yu, Russell D. Wolfinger, C. Vens, Leander Schietgat, Kurt De Grave, Raquel Norel, Gustavo Stolovitzky, Guillermo A. Cecchi, and Leslie B. Vosshall. Predicting human olfactory perception from chemical features. *Science*, 355(6327):820–826, 2017.
- [2] K. J. Rossiter. Structure–odor relationships. *Chemical Reviews*, 96(8):3201–3240, 1996.
- [3] M. Devos, F. Patte, J. Rouault, P. Laffort, and L. J. Van Gemert. *Standardized Human Olfactory Thresholds*. Oxford University Press, Oxford, UK, 1990.
- [4] David Rogers and Mathew Hahn. Extended-connectivity fingerprints. *Journal of Chemical Information and Modeling*, 50(5):742–754, 2010.
- [5] Justin Gilmer, Samuel S. Schoenholz, Patrick F. Riley, Oriol Vinyals, and George E. Dahl. Neural message passing for quantum chemistry. In *Proceedings of the 34th International Conference on Machine Learning (ICML)*, volume 70 of *PMLR*, pages 1263–1272, 2017.
- [6] Keyulu Xu, Weihua Hu, Jure Leskovec, and Stefanie Jegelka. How powerful are graph neural networks? In *International Conference on Learning Representations (ICLR)*, 2019.
- [7] Weihua Hu, Bowen Liu, Joseph Gomes, Marinka Zitnik, Percy Liang, Vijay Pande, and Jure Leskovec. Strategies for pre-training graph neural networks. In *International Conference on Learning Representations (ICLR)*, 2020.
- [8] Gabriele Corso, Luca Cavalleri, Dominique Beaini, Pietro Lió, and Petar Veličković. Principal neighbourhood aggregation for graph nets. In *Advances in Neural Information Processing Systems (NeurIPS)*, 2020.
- [9] G. W. Bemis and M. A. Murcko. The properties of known drugs: Molecular frameworks. *Journal of Medicinal Chemistry*, 39(15):2887–2893, 1996.

- [10] Robert P. Sheridan. Time-split cross-validation as a method for estimating the goodness of prospective prediction. *Journal of Chemical Information and Modeling*, 53(4):783–790, 2013.
- [11] Zhenqin Wu, Bharath Ramsundar, Evan N. Feinberg, Joseph Gomes, Caleb Geniesse, Aneesh S. Pappu, Karl Leswing, and Vijay Pande. Moleculenet: A benchmark for molecular machine learning. *Chemical Science*, 9(2):513–530, 2018.
- [12] Kevin Yang, Kyle Swanson, Wengong Jin, Connor Coley, Philipp Eiden, Hua Gao, Alberto Guzman-Perez, Trevor Hopper, Bryan Kelley, Marius Mathea, Andrew Palmer, Volker Settels, Tommi Jaakkola, Klavs F. Jensen, and Regina Barzilay. Analyzing learned molecular representations for property prediction. *Journal of Chemical Information and Modeling*, 59(8):3370–3388, 2019.
- [13] Rich Caruana. Multitask learning. *Machine Learning*, 28(1):41–75, 1997.
- [14] Sebastian Ruder. An overview of multi-task learning in deep neural networks, 2017.
- [15] Yao Xu, Junshui Ma, Andy Liaw, Robert P. Sheridan, and Vladimir Svetnik. Demystifying multitask deep neural networks for quantitative structure–activity relationships. *Journal of Chemical Information and Modeling*, 57(10):2490–2504, 2017.
- [16] Trevor Standley, Amir Roshan Zamir, Dawn Chen, Leonidas Guibas, Jitendra Malik, and Silvio Savarese. Which tasks should be learned together? In *Proceedings of the 37th International Conference on Machine Learning (ICML)*, volume 119 of *PMLR*, pages 9120–9132, 2020.
- [17] Ozan Sener and Vladlen Koltun. Multi-task learning as multi-objective optimization. In *Advances in Neural Information Processing Systems (NeurIPS)*, volume 31, pages 525–536, 2018.
- [18] Tianhe Yu, Saurabh Kumar, Abhishek Gupta, Sergey Levine, Karol Hausman, and Chelsea Finn. Gradient surgery for multi-task learning. In *Advances in Neural Information Processing Systems (NeurIPS)*, volume 33, pages 5824–5836, 2020.
- [19] Alex Kendall, Yarin Gal, and Roberto Cipolla. Multi-task learning using uncertainty to weigh losses for scene geometry and semantics. In *Proceedings of the IEEE/CVF Conference on Computer Vision and Pattern Recognition (CVPR)*, pages 7482–7491, 2018.
- [20] Nathan Brown, Peter Ertl, Richard Lewis, Thomas Luksch, Daniel Reker, and Gisbert Schneider. *Future Directions of Chemoinformatics: Ensembles of ML, Big Data, and Graphs*. Springer, 2017.
- [21] Petar Veličković, Guillem Cucurull, Arantxa Casanova, Adriana Romero, Pietro Lio, and Yoshua Bengio. Graph attention networks. In *International Conference on Learning Representations (ICLR)*, 2018.

- [22] Kristof T. Schütt, Huziel E. Sauceda, Pieter-Jan Kindermans, Alexandre Tkatchenko, and Klaus-Robert Müller. Schnet: A continuous-filter convolutional neural network for modeling quantum interactions. *Journal of Chemical Physics*, 148(24):241722, 2018.
- [23] Chengxuan Ying, Tianle Cai, Shengjie Luo, Shuxin Zheng, Guolin Ke, Di He, Yanming Shen, and Tie-Yan Liu. Do transformers really perform badly for graph representation? In *NeurIPS*, 2021.
- [24] Fan-Yun Sun, Jordan Hoffmann, Vikas Verma, and Jian Tang. Infograph: Unsupervised and semi-supervised graph-level representation learning via mutual information maximization. In *International Conference on Learning Representations (ICLR)*, 2020.
- [25] Yu Rong, Yatao Bian, Tingyang Xu, Weiyang Xie, Ying Wei, Wenbing Huang, and Junzhou Huang. Self-supervised graph transformer on large-scale molecular data. In *Advances in Neural Information Processing Systems (NeurIPS)*, 2020.
- [26] Kevin Yang, Kyle Swanson, Wengong Jin, Connor Coley, Philipp Eiden, Hua Gao, Alberto Guzman-Perez, Trevor Hopper, Bryan Kelley, Marius Mathea, Andrew Palmer, Volker Settels, Tommi Jaakkola, Klavs F. Jensen, and Regina Barzilay. Analyzing learned molecular representations for property prediction. *Journal of Chemical Information and Modeling*, 59(8):3370–3388, 2019.
- [27] Yu Rong, Wenbing Huang, Tingyang Xu, and Junzhou Huang. Dropedge: Towards deep graph convolutional networks on node classification. In *International Conference on Learning Representations (ICLR)*, 2020.
- [28] Pavel Izmailov, Dmitry Podoprikin, Timur Garipov, Dmitry Vetrov, and Andrew Gordon Wilson. Averaging weights leads to wider optima and better generalization. In *UAI*, 2018.
- [29] Boris T. Polyak and Anatoli B. Juditsky. Acceleration of stochastic approximation by averaging. *SIAM Journal on Control and Optimization*, 30(4):838–855, 1992.
- [30] Weihua Hu, Matthias Fey, Marinka Zitnik, Yuxiao Dong, Hongyu Ren, Bowen Liu, Michele Catasta, and Jure Leskovec. Open graph benchmark: Datasets for machine learning on graphs. In *NeurIPS*, 2020.
- [31] Frederik H. Vermeire and William H. Green. Transfer learning in chemical engineering with limited data: Mind the time split. *Engineering Applications of Artificial Intelligence*, 113:104911, 2022.
- [32] Marcel Böckmann, Thilo Wackersreuther, Frank Driller, Klaus-Robert Müller, and Francesco Montanari. On the pitfalls of molecular property prediction: Data leakage, split strategies and realistic benchmarks. *Journal of Cheminformatics*, 15(1):122, 2023.
- [33] Joel D. Mainland, Johan N. Lundström, Johannes Reisert, and Graeme Lowe. From odor molecules to perception: Olfactory signal transduction and coding. *Annual Review of Physiology*, 76:307–327, 2014.

- [34] Peter J. Huber. Robust estimation of a location parameter. *Annals of Mathematical Statistics*, 35(1):73–101, 1964.
- [35] Peter J. Huber and Elvezio M. Ronchetti. *Robust Statistics*. Wiley, 2nd edition, 2009.
- [36] Frederick Mosteller and John W. Tukey. *Data Analysis and Regression*. Addison-Wesley, 1977.
- [37] Wang Zhang, Lihua Deng, Lei Zhang, and Di Wu. A survey on negative transfer. *IEEE/CAA Journal of Automatica Sinica*, 10(3):305–329, 2022.
- [38] Zhao Chen, Vijay Badrinarayanan, Chen-Yu Lee, and Andrew Rabinovich. Gradnorm: Gradient normalization for adaptive loss balancing in deep multitask networks. In *International Conference on Machine Learning (ICML)*, pages 794–803, 2018.
- [39] Shikun Liu, Edward Johns, and Andrew J. Davison. End-to-end multi-task learning with attention. In *IEEE/CVF Conference on Computer Vision and Pattern Recognition (CVPR)*, pages 1871–1880, 2019.
- [40] David A. Nix and Andreas S. Weigend. Estimating the mean and variance of the target probability distribution. *Proceedings of the IEEE International Conference on Neural Networks*, 1:55–60, 1994.